Author Manuscript

Author Manuscript

Author Manuscript

Author Manuscript

HHS Public Access

Author manuscript

Med Phys. Author manuscript; available in PMC 2018 October 01.

Published in final edited form as:

Med Phys. 2017 October ; 44(10): 5128–5142. doi:10.1002/mp.12396.

A Random Walk-based Segmentation Framework for 3D Ultrasound Images of the Prostate

Ling Ma[1], **Rongrong Guo**[1], **Zhiqiang Tian**[1], and **Baowei Fei**[1,2,3,4,*]

[1]Department of Radiology and Imaging Sciences, Emory University School of Medicine, Atlanta, GA 30329

[2]The Wallace H. Coulter Department of Biomedical Engineering, Emory University and Georgia Institute of Technology, Atlanta, GA 30329

[3]Winship Cancer Institute of Emory University, Atlanta, GA 30329

[4]Department of Mathematics and Computer Science, Emory College of Emory University, Atlanta, GA 30329

Abstract

Purpose—Accurate segmentation of the prostate on ultrasound images has many applications in prostate cancer diagnosis and therapy. Transrectal ultrasound (TRUS) has been routinely used to guide prostate biopsy. This manuscript proposes a semiautomatic segmentation method for the prostate on three-dimensional (3D) TRUS images.

Methods—The proposed segmentation method uses a context-classification based, random walk algorithm. Because context information reflects patient-specific characteristics and prostate changes in the adjacent slices, and classification information reflects population-based prior knowledge, we combine the context and classification information at the same time in order to define the applicable population and patient-specific knowledge so as to more accurately determine the seed points for the random walk algorithm. The method is initialized with the user drawing the prostate and non-prostate circles on the mid-gland slice and then automatically segments the prostate on other slices. To achieve reliable classification, we use a new adaptive k-means algorithm to cluster the training data and train multiple decision tree classifiers. According to the patient-specific characteristics, the most suitable classifier is selected and combined with the context information in order to locate the seed points. By providing accuracy locations of the seed points, the random walk algorithm improves segmentation performance.

Results—We evaluate the proposed segmentation approach on a set of 3D TRUS volumes of prostate patients. The experimental results show that our method achieved a Dice similarity coefficient of 91.0% ± 1.6% as compared to manual segmentation by clinically experienced radiologist.

Conclusions—The random walk based segmentation framework, which combines patient-specific characteristics and population information, is effective for segmenting the prostate on

*Corresponding author: Baowei Fei, Ph.D., Department of Radiology and Imaging Sciences, Emory University School of Medicine, 1841 Clifton Road NE, Atlanta, GA 30329, bfei@emory.edu, Phone: 404-712-5649, Website: www.feilab.org.

Author Manuscript Author Manuscript Author Manuscript Author Manuscript

ultrasound images. The segmentation method can have various applications in ultrasound-guided prostate procedures.

Keywords

Image segmentation; context; classification; random walk; transrectal ultrasound (TRUS); prostate cancer

I. INTRODUCTION

Prostate cancer is one of the major causes of cancer mortality in American men, and it is estimated that there were 180,890 new cases of prostate cancer in the United States in 2016, and which accounts for 21% of all cases in men.[1] Transrectal ultrasound (TRUS) guided biopsy is the standard care for definitive diagnosis of prostate cancer.[2, 3] Three-dimensional (3D) TRUS can provide 3D visualization of the prostate and its combination with magnetic resonance imaging (MRI) has been used to improve the detection of prostate cancer.

Accurate prostate segmentation in 3D TRUS images can provide an accurate measurement of the prostate volume. After segmentation, the 3D model of the prostate can be used for the planning of MRI/TRUS fusion guided biopsy. Segmentation of the prostate can also be used in brachytherapy planning. As manual segmentation is time-consuming and relies upon the experience of the clinician, automatic or semiautomatic segmentation can have much value in clinical applications. Various efforts have been made to segment the prostate on ultrasound images,[4] which include the contour-based methods, region-based methods, classification-based methods, and hybrid methods, as described in the following section.

The contour-based methods use the prostate boundary or edge information to guide the segmentation.[5–23] As they depend on reliable edge information, they may be adversely affected by the presence of shadow artifacts seen on the ultrasound images.[24] The region-based methods use the predominant intensity distributions of the prostate region to guide the segmentation.[25–27] They may, however, show an incomplete prostate region because the prostate is not uniform. The classification-based methods use features extracted from ultrasound images to cluster or classify the image into the prostate and non-prostate.[28] Because of intensity heterogeneity and unreliable texture, a pure, classification-based segmentation method can have difficulties to reliably segment the prostate gland on ultrasound images. Therefore, the segmentation methods based on a single type of information, such as the contour, region or classification information, may make it difficult to achieve satisfactory performance in the practical applications.

Hybrid-based methods can maximize the advantage of each type of information by combining multiple kinds of information, such as contour, region, and/or classification, in order to segment the prostate.[29–37] Akbari *et al.* combined the statistical shape (contour information), classification information, and intensity profiles (region information) to complete the prostate segmentation. In the first step, they trained a set of wavelet support vector machines (SVM) to adaptively capture the features of the ultrasound images in order to differentiate the prostate and non-prostate tissue. In the second step, they modified the surfaces based on the shape model and intensity profiles. These two steps are repeated until

Author Manuscript Author Manuscript Author Manuscript Author Manuscript

they converge to get the final segmented prostate.[29–32] In another study, an energy function was proposed to combine a shape model and region-based information in a Bayesian framework in order to segment the 3D prostate in a level-set framework.[33] In another automatic 3D segmentation method, statistical textures were obtained from Gabor filters, and multi-atlas registration and SVMs were used to segment the prostate.[34] Zhan *et al.* trained the SVMs to measure the probability of voxels belonging to the prostate and used those classification results to define an energy function in order to drive the surface of the deformable model for the prostate segmentation.[35, 36] They also used a Zernike moment-based edge detector for boundary identification and designed a new SVM training method for effectively reducing the number of support vectors.[37] Multi-atlas registration and anatomical signatures were also used for the segmentation of the prostate on ultrasound images.[38]

Although the hybrid-based methods may be able to improve segmentation performance because of the combination of multiple information, the existing hybrid methods still suffer from two problems: 1) They depend on the population data and use the shape model or atlas obtained from the population to guide the segmentation of the prostate; and 2) They may be not robust due to the low signal-to-noise ratio for ultrasound image. For example, level-set-based methods can be affected by the speckles on TRUS images, and thus leading to segmentation leakage.

In this manuscript, we introduce a hybrid algorithm combining the region and classification information for the segmentation of the prostate on ultrasound images. On the one hand, we cluster the population data using a new adaptive k-means method and then train multiple classifiers. For a new patient, we use the patient-specific character to choose the most suitable classifier to obtain the classification information. Although we still use the population information for the segmentation, we analyze the relationship between the population and patient-specific character for selecting applicable population knowledge for prostate segmentation. On the other hand, a random walk algorithm may have the attractive advantage that it can avoid segmentation leakage and shrinking bias and is thus robust to the low-contrast, speckle microcalcifications and imaging artifacts on the ultrasound images.[38, 39] Therefore, we choose the random walk method to express the region information. Our method uses both the population and patient-specific character to determine the prostate and non-prostate pixels, and the prostate and non-prostate pixels are chosen as the seed points for initialization of the random walk algorithm for the prostate segmentation.

The proposed segmentation method is significant expansion of our preliminary study[41] in the following aspects: (1) This proposed method involved an applicable population model selection method. We train multiple classifiers during the training procedure. For a new patient, we compare the patient-specific character and population character and select the best-match population knowledge for the patient-specific segmentation; (2) We tested whether the proposed method is sensitive to the user interaction and demonstrated that the method was robust and insensitive to the user interaction; (3) We significantly expanded the Introduction section and also included more details in the sections regarding the method, theoretical analysis, implementation, and comprehensive experiments; (4) We added a

Author Manuscript Author Manuscript Author Manuscript Author Manuscript

Discussion section to investigate several, related problems; and (5) We used more measurements to evaluate the performance of the method.

The main contributions of this paper are summarized as follows: 1) We proposed a context-classification based, random walk algorithm for the prostate segmentation. The random walk algorithm can avoid discretization errors, segmentation leakage, and shrinking bias in order to improve segmentation accuracy. To the best of our knowledge, our proposed random walk algorithm is used for the first time, for prostate segmentation on 3D ultrasound images; 2) We reduce user interaction. Instead of locating the seed points on all image slices by user, we just need the user interaction for the mid-gland slice. The applicable population and patient-specific knowledge is used to automatically determine the seed points on the other slices. It can improve the accuracy of the location of the initial seed points without the help of the user interaction and thus improve segmentation performance; and 3) Clinical data have demonstrated the robustness and accuracy of the proposed segmentation method that can be of particularly useful for our 3D TRUS-guided prostate biopsy application.

II. METHOD

We propose a new segmentation method for the prostate in 3D TRUS images by using a context-classification based, random walk algorithm which is called C-RW for short and is illustrated in Fig. 1. Our method includes two stages, *i.e.* the training and the segmentation stages. In the training stage, we cluster the dataset of manually segmented ultrasound images by radiologist, *i.e.*, atlases, into k clusters, where k is an adaptive parameter. Then we extract the pixel features from the corresponding ultrasound images in each cluster to train the classifier. Therefore, we can get the k classifiers during the training process. In the segmentation stage, we perform the 3D segmentation by segmenting the prostate on each 2D slice. 1) For a new patient, we first initialize our algorithm with the user selecting the start and end slice of the prostate and drawing the fore- and background circles on the mid-gland slice, which correspond to the prostate and non-prostate regions, respectively. Based on these contour points, we run the random walk algorithm to segment the prostate on the mid-gland slice and obtain the 2D segmented prostate mask. 2) We align the mask with the atlases in k clusters and select the closest cluster according to their overlap areas. 3) We compute the fore- and background seed points on the adjacent slice and segment the prostate until all slices were segmented. The details of the two stages are described in the following sections.

A. Train the k Decision Tree Classifiers

In the training stage, our objective is to obtain the classifiers to guide the prostate segmentation. As the prostates of different patients have different appearances, and even the prostate of the same patient could appear to have different shapes or sizes due to the patient's position and condition, we train multiple classifiers to distinguish the prostate and non-prostate tissue. We cluster the dataset of the atlases by using a new, adaptive k-means method, and then extract the features from the corresponding ultrasound images in each cluster to train the classifiers.

Author Manuscript Author Manuscript Author Manuscript Author Manuscript

1) Registration of the Atlases—In order to obtain more accurate separation of 3D atlases, we pre-process the atlases to make them aligned in the same area and in the same orientation by using a registration procedure. We randomly select one 3D atlas as the fixed image and align the other 3D atlases (called the moving image) with the fixed one by using an intensity-based, image registration method. In this manuscript, we use the rigid transformation type and the mutual information as the similarity measure. We can obtain the optimized, transformed images when the registration process has reached the specified maximum number of iterations, 300.

2) Adaptive k-means Clustering—We used a k-means clustering method to automatically partition population data set k groups.[42] The k-means algorithm has the advantage of favorable execution time and better performance, but it also has the disadvantage that the quality of the final clusters depends on the choice of k. Therefore, we proposed an adaptive k-means algorithm where k is an adaptive value according to the property of data. For clustering, we generally attempted to maximize intra-class similarity and inter-class differences. As the Fisher criterion can maximize the inter-class scatter over intra-class scatter,[43] we used the Fisher criterion to evaluate the cluster performance with respect to k and chose the k with the best clustering performance. Let X_i^j be the feature of the *j*-th sample in the *i*-th cluster and N_i be the number of features in the *i*-th cluster. We can compute the mean of each cluster M_i:

$$M_i = \frac{1}{N_i} \sum_{j=1}^{N_i} X_i^j, \quad (1)$$

and the mean of all features M as

$$M = \frac{\sum_{i=1}^{k} \sum_{j=1}^{N_i} X_i^j}{\sum_{i=1}^{k} N_i}. \quad (2)$$

Then, the intra-class distance D_{intra} can be determined by

$$D_{\text{intra}} = \sum_{i=1}^{k} \frac{1}{N_i} \sum_{j=1}^{N_i} \left\| X_i^j - M_i \right\|^2. \quad (3)$$

and the inter-class distance D_{intra} can be determined by

$$D_{\text{inter}} = \sum_{i=1}^{k} \left\| M_i - M \right\|^2. \quad (4)$$

Finally, the criterion function $f(k)$ is computed as

Author Manuscript Author Manuscript Author Manuscript Author Manuscript

$$f(k)=\frac{k}{D_{\text{inter}}/D_{\text{intra}}}. \quad (5)$$

And the optimal k is computed by

$$k^{*}=\arg\ \min\ f(k). \quad (6)$$

The numerator of the criterion function is the number of the clusters. Obviously, the better generalization ability the k-mean method has, the smaller this value is, and the smaller the function value is. In the denominator, we consider the performance clustered by the k-mean method. Since the denominator indicates the discriminate results to the distances between the intra-class and inter-class clusters, the larger discriminate value proves that the k-mean with the k has a better cluster separation. Therefore, the smaller $f(k)$ indicates the better clustering performance.

We compute the minimum bounding rectangle of the prostate for the aligned atlases and then extract the length, width, and height of the rectangle as well as the number of pixels belonging to the 3D prostate as their features. We use the k-means with k from 2 to N/2 (N is the number of training data) to cluster these features and use the criterion function in (5) to value the clustering performance. We chose the best k according to the minimum value of $f(k)$.

3) Extract the Features—We need to choose the adaptive feature description in order to distinguish between prostate and non-prostate pixels. The local binary patterns (LBP) value is a highly discriminative texture descriptor and is insensitive to gray scale change.[44] The LBP describe the relationship between a center pixel and its surrounding neighbors. For a 3 × 3 neighboring condition, the LBP can be computed as

$$\text{LBP}(c)=\sum\nolimits_{n=0}^{7} G(I_c - I_n) \times 2^n, \quad (7)$$

where I_c and I_n are the intensity of the center pixel and its neighborhood pixel and $G(x)$ is a threshold, as defined by

$$G(x)=\begin{cases} 1, & x \geq 0 \\ 0, & x<0 \end{cases}. \quad (8)$$

In (7), the original neighborhood is thresholded by the intensity value of the center pixel. Those binary values are then converted to decimal for convenience as the LBP value of this center pixel.

Author Manuscript Author Manuscript Author Manuscript Author Manuscript

Since LBP is a highly discriminative texture descriptor, location information can indicate the probability of a pixel belonging to the prostate and the intensity information can reflect the local spatial variation in the boundary, we extract the three types of features for each pixel in the corresponding ultrasound images in each cluster. Specifically, the location feature is represented by the x, y, and z coordinates of the pixel, the intensity feature is the intensity value of the pixel, and the LBP feature is the LBP value calculated in (7). Fig. 2 shows the original images in sagittal, transverse, and coronal directions and their LBP features.

4) Train the Decision Tree—Based on these features, we train a classifier. The decision tree is the classifier that has fast speed and superior performance, especially for a binary classification problem.[45] The decision-tree classifier is a tree which consists of a root node, several interior nodes, and leaf nodes. The objective of the decision tree algorithm is to grow into a tree, where the root node is the entire set of classes, whereas the terminal nodes represent the final classification results by splitting the nodes based on training samples and their labels. The split criterion is the discrimination ability measured by the purity measure and a single feature. Therefore, in each split process, it chooses the split which can maximize the difference of the impurity of the parent node t and its child nodes t_l and t_r such that

$$\Delta(t)=p(t)-f_l^{p(t_l)}-f_r^{p(t_r)}, \quad (9)$$

where $p(t)$ is the purity of the node t and f_l and f_r are the features that reach into the left child t_l and right child t_r.

Since decision tree classifier, which has been widely applied to medical image classification, does not rely on any prior statistical assumption, we utilize the decision tree as the classifier and train a decision tree in each cluster. We then have k classifiers during the training process.

B. Random Walk-based Segmentation

In the segmentation stage, given a new patient, we perform the segmentation from the middle to both the apex and base slices until all slices are segmented. We then combine and smooth these 2D prostate masks to achieve a 3D-segmented prostate.

1) Random Walk—The random walk algorithm is an interactive segmentation method. Fig. 3 shows the flowchart of the random walk algorithm for segmentation. After the user marks the foreground and background seed points, the method constructs a weighted graph with the vertices corresponding to the pixels on the image and the edges representing the distance between connected vertices. The weighted value of edges can be calculated by

$$E(i,j)=\exp(-\beta(I_i-I_j)^2), \quad (10)$$

where I_i is the intensity of vertix i, and β is a free parameter to which we set 90 in our experiments according to Ref. 39. The random walk method performs segmentation by

Author Manuscript Author Manuscript Author Manuscript Author Manuscript

computing the probabilities of unlabeled points first arriving at the seed points and by choosing the highest probability as the label. As the solution of the probability computation has been found to be the same as minimizing a combinatorial Dirichlet problem, we generate the Laplacian matrix to transform it into the Dirichlet problem for a partition.

A random walk is the process by which randomly moving objects wander away. Although it uses the image intensity to compute the edge weight, it takes the weight as the likelihood that a random walker will go across that edge. Based on randomness, random walker is more likely to reach the seed with the least steps and thus might avoid segmentation leakage and shrinking bias.

In this manuscript, we choose a 2D random walk algorithm to segment the prostate slice by slice because a 3D random walk will require more initial seed points and running time and has less than unity probability of reaching any point, including the starting point, as the number of steps approach infinity, while the 1D and 2D random walk have unity probability of reaching the starting point.[46]

2) Initialization—The user first selects the starting slice at the base of the prostate and the ending slice at the prostate apex. A slice at the mid-gland is then selected and the user draws the fore- and background circles according to the prostate and non-prostate regions. Based on these seed points on the circles, we run the 2D random walk algorithm to segment the prostate on the mid-gland slice and get its mask.

3) Classifier Selection—According to the mask on the mid-gland slice, we select the best suitable classifier from k classifiers. In each cluster, we align our mask with each of the 2D atlases on the mid-gland slice and compute the sum of their overlap areas as the similarity measure. With the maximum sum of the overlap areas, we obtain the closest cluster and its corresponding classifier from the k classifiers. We then use the transform matrix to transform the other slices to make them consistent with the training model.

4) Determine the Seed Points by Combining the Context and Classification Information—The important step is the determination of the initial seed points for the random walk algorithm because the user just marks the seed points on one slice. To obtain the highly accurate location information regarding the seed points, we combine the context and classification information in order to determine the location of the seed points.

The context information represents the patient-specific information obtained by the segmented mask on the adjacent slice. We assume that the difference between the shape and size of the prostate on the two adjacent slices is not likely to be large. Morphology is a broad set of image processing operations based on shapes.[47] We use morphological operations to process the mask. Dilation can expand the object in an image, whereas erosion can shrink the objects. Therefore, we use the dilation and erosion operations to expand and shrink the mask on the adjacent slice. The fore- and background points on the adjacent slice are then used as the fore- and background points on the current slice, respectively. We provide an example with the size of five pixels in Fig. 4, where the solid red, dot green, and dash blue lines indicate the segmented mask on the adjacent slice, the shrunk mask, and the expanded

Author Manuscript Author Manuscript Author Manuscript Author Manuscript

mask, respectively. We use the pixels inside the shrunk mask as the foreground points, as shown by the green points, and the pixels outside the expanded mask as the background points, as shown by the blue points. After the dilation and erosion operations, we obtain the fore- and background points and the probability of each pixel. In order to achieve a good performance, we decide the size of the expansion or the shrinking by segmentation experiments.

The classification information indicates the population information obtained by the trained classifier. Because the appearance, including the shape and size, of the prostate both in the base and apex regions differs from that in the mid-gland region and because the context information slightly changes the appearance of the segmented prostate, it is difficult to obtain a good segmentation performance based only on the context information. To overcome this problem, we involve the classification information to segment the prostate in the base and apex regions. We choose the best classifier and compute the probability of each pixel belonging to the prostate and non-prostate. Then we choose the pixels in which probabilities of belonging to the prostate are equal to 1 as the foreground seed points, and choose the pixels in which the probabilities of belonging to prostate are equal to 0, as the background seed points. Therefore, the number of seed points is not fixed and is a case-specific number.

By combining the probability obtained by the two types in a weighted-sum form, we determine the final probability of each pixel. Let $P_f^1(i)$ and $P_b^1(i)$ be the probability of pixel i belonging to the fore- and background points according to the context information, respectively, $P_f^2(i)$ and $P_b^2(i)$ be the probability according to the classification result, and $P_f(i)$ and $P_b(i)$ be the final probability of being the prostate and non-prostate for pixel i, and they are computed by

$$P_f(i)=w_1 \times P_f^1(i)+w_2 \times P_f^2(i),$$

$$P_b(i)=w_1 \times P_b^1(i)+w_2 \times P_b^2(i) \quad (11)$$

where w_1 and w_2 is the weight assigned to the probability obtained by the context and classification information, respectively, and they are determined by

$$w_1=f(\exp(\mathrm{Va}), \frac{\mathrm{Dslice}}{\mathrm{ABslice}}),$$

$$w_2=1-w_1 \quad (12)$$

where the *Dslice* is the absolute difference between the number of current slices and mid-gland slices, the *ABslice* is the absolute difference between the number of apex and base

Author Manuscript Author Manuscript Author Manuscript Author Manuscript

slices, and the $f(.)$ is an exponential function. Fig. 5 shows the base, mid-gland, apex, and the current slices, and what the *Dslice* and *ABslice* is. Therefore, $\frac{\mathrm{Dslice}}{\mathrm{ABslice}}$ must be a positive number less than 1. The parameter Va, a coefficient to make a tradeoff between the impacts of the two factors, is determined by experiments. If we set Va to a minus value, we can get a decreasing function. If the slice to be segmented is far from the mid-gland slice, the value of the *Dslice* is large. Therefore, the value of w_1 is becoming smaller and which means that the influence of the context information becomes less important and the classification information more important. Then we choose the numbers of the fore- and background seed points, N_f and N_b, in the descending order of final probability, and which are determined by

$$N_f = \mathrm{round}(w_1 \times N_f^1 + w_2 \times N_f^2),$$

$$N_b = \mathrm{round}(w_1 \times N_b^1 + w_2 \times N_b^2). \quad (13)$$

where N_f^1 and N_b^1 are the total number of fore- and background points obtained by the context information, N_f^2 and N_b^2 are the total number of fore- and background points obtained by the classification decision, and the $round(\cdot)$ is the nearest integer function to ensure that the number of foreground and background points is an integer.

5) Segmentation of the 3D prostate—Based on the seed points, we run the random walk method for the 2D prostate segmentation and propagate the process until all of the slices have been segmented. We then combine all the 2D prostate masks to form a 3D segmented prostate. And we use the Gaussian smooth with a fixed size of 5 pixels as the size of the convolution kernel to smooth the 3D prostate.

C. Evaluation Criteria

The performance of the algorithm is evaluated against the clinical gold-standard by computing the volumetric and surface-based distance measures. We use the Dice similarity coefficient (DSC), sensitivity, specificity, detection, false negative rate (FNR), and overlap error (OVE), to quantify shape similarity between our segmented prostate and the gold-standard. And we calculate the Hausdorff distance (HD) between them to quantify the surface distance.[48]

The Dice similarity coefficient is the relative volume overlap between S and G, where S and G are the binary masks from our method and gold standard established by expert-defined segmentation, respectively. The DSC can be computed as:

$$\mathrm{DSC} = \frac{2 \times \mathrm{TP}}{(\mathrm{FP}+\mathrm{TP})+(\mathrm{TP}+\mathrm{FN})}, \quad (14)$$

Author Manuscript Author Manuscript Author Manuscript Author Manuscript

where TP, TN, FP, FN are the number of true positives, true negatives, false positives, and false negatives, respectively. “True positive” means that the pixels are correctly classified as the prostate. If a prostate pixel is incorrectly classified as a non-prostate, we call it “false negative”. In the same way, “true negative” means that a non-prostate pixel is correctly classified as non-prostate, whereas “false positive” means that a non-prostate pixel is correctly classified as the prostate.

Sensitivity measures the proportion of actual positives which are correctly identified as the prostate, and specificity measures the proportion of negatives which are correctly identified as non-prostate. They are determined by:

$$\text{Sensitivity}=\frac{\text{TP}}{\text{TP}+\text{FN}}.$$

$$\text{Specificity}=\frac{\text{TN}}{\text{TN}+\text{FP}} \quad (15)$$

Detection is calculated as

$$\text{Detection}=\frac{\text{TP}}{\text{FP}+\text{FN}}. \quad (16)$$

The false negative rate is defined as the number of false negative voxels divided by the total number of the prostate voxels on the gold standard and is computed by

$$\text{FNR}=\frac{\text{FN}}{\text{TP}+\text{FN}}. \quad (17)$$

The overlap error is determined by determining the non-overlap area between the segmented result and the gold standard:

$$\text{OVE}=1-\frac{S\cap G}{S\cup G}. \quad (18)$$

Hausdorff distance measures how far two subsets of points are obtained by our proposed method and gold standard and is defined as

$$d_H(S,G)=\{\sup_{s\in S}\inf_{g\in G}d(s,g),\sup_{g\in G}\inf_{s\in G}d(s,g)\}, \quad (19)$$

where *sup* and *inf* represent the supremum and infimum, respectively.

Author Manuscript Author Manuscript Author Manuscript Author Manuscript

III. EXPERIMENTS AND RESULTS

A. Database

We collected 32 3D transrectal ultrasound image volumes from 16 clinical patients who underwent prostate biopsy. Each patient had two image volumes acquired at different times. An ultrasound system and an end-firing, 5–9 MHz, TRUS transducer were used for the image acquisition. The voxel size of the image was 0.19 mm × 0.19 mm × 0.19 mm, and the size of the images was 448×448×350 voxels. The prostate was manually segmented on each image slice by an experienced clinic radiologist in order to produce the gold standard for evaluation. We conducted leave-one-out style, cross-validation experiments for the prostate segmentation method. We take each of 32 TRUS image volumes as the testing image to be segmented in turn, and the remaining 31 ones as the training samples.

B. Parameter Tuning

The two parameters of our approach, which are described in Section II, were set up through experiments. The first parameter is the size of the dilation and erosion processing. As a too large or small value of the size leads to errors in the prostate location, we tested 20 integers from 1 to 20 pixels and selected the one with the best performance. For each tested number, we just used the context information to choose the fore- and background seed points and run the random walk algorithm for the prostate segmentation. As shown in Fig. 6, the results demonstrated that the optimal size is 4 pixels, *i.e.*, 0.76 mm. This number is used in all of the following experiments.

The second parameter is the parameter Va in (12), which is a coefficient to make a tradeoff between the impacts of the context information and the classification information. We performed our method with 20, different Va from −20 to −1 and show these results in Fig. 7. From Fig. 7, we choose −6 for Va because it gives the best performance.

C. Qualitative Evaluation Results

The segmentation results from three prostate volumes are shown in Fig. 8. The solid blue curves are the manual segmentation performed by the radiologist and were used as the gold standard. The dash red curves are segmented by the proposed method. We show the 2D segmented results in the base, mid-gland, and apex regions. The segmented boundaries are close to the gold standard and demonstrate the effectiveness of the segmentation method.

D. Quantitative Evaluation Results

Table I shows the mean and standard deviation of the segmented results as measured by seven metrics for 32 volumes. Each volume is divided into three sub-regions that include the apex, mid-gland, and the base regions. The three sub-regions contain the 30%, 40%, and 30% slices of the whole prostate, respectively. The segmentation method achieved a DSC of 91.0±1.6% for the whole gland, and thus indicating a high segmentation accuracy and a small standard deviation. For the 32 volumes, we use the Hausdorff distance to measure the maximum distance in mm between the two surfaces of the prostate, and which were segmented by our proposed method and by an experienced radiologist. We obtained the Hausdorff distance of 8.9±1.4 mm. The results in the apex and base regions are not as

Author Manuscript Author Manuscript Author Manuscript Author Manuscript

positive as those of the mid-gland region because it is difficult to segment the apex and base regions. The quantitative evaluation results demonstrate that our method achieved a satisfactory segmentation performance.

E. The Effectiveness of the Proposed Method

First we tested the performance of multiple classifiers. To better describe the diversity of the prostate, we train multiple classifiers with the help of the clustering method based on different shapes and sizes of the prostates. We compare our multiple classifiers with the single classifier in order to show our advantage. For our multiple classifiers and a test sample, the best classifier is chosen and used to classify the test sample. For the single classifier, all of the training samples are used to train a model and the model is then used for the classification. We provided the results in Fig. 9 which showed the improvement of the segmentation accuracy with our multiple classifiers as compared with one classifier. We recorded the Fisher values for the leave-one-out cross validation experiments and choose the best k as 6, 6, 5, 6, 7, 6, 5, 6, 6, 7, 6, 6, 6, 6, 6, 6, 5, 7, 8, 5, 5, 7, 5, 6, 5, 5, 5, 7, 6, 7, 6, and 5, respectively.

Secondly, we compared the three approaches: intensity only; LBP only; and the combination of intensity and LBP, for the training. The classification accuracy is shown in Fig. 10. LBP can achieve better classification accuracy than the intensity feature. Our combined method achieves the highest accuracy, and the combined feature can best distinguish the prostate and non-prostate pixels with the classification.

Thirdly, our method combines the context and classification information in order to determine the seed points for the random walk algorithm. In order to demonstrate the usefulness of the combination, we compare it using two methods: one only uses the context information to determine the seed points for the random walk algorithm (CO-RW); and the other one only uses classification information (CL-RW). In our experiments, we segmented the prostate for the 32 volumes by using the CO-RW, CL-RW, and our method.

We provide the location of the seed points determined by the CO-RW, CL-RW, and our method on one image slice in Fig. 11, where the white points indicate the foreground points and the black points indicate the background points, the solid blue contours are the manually segmented gold standard, and the dash red contours are our segmented results. Fig. 11 demonstrates that the object segmented by CO-RW has some location errors and the object segmented by CL-RW contains some irrelevant regions, while the object segmented by our combined method is closed to the gold standard. Our combined context-classification can locate the seed points more accurately.

In addition, we present the segmentation results in Fig. 12. The average DSC using our method is 91.0%, and which is better than the CO-RW method of 75.35% or the CL-RW method of 80.65%. The results demonstrated that our method performs better than either the CO-RW or CL-RW method. Our method combines their advantages and overcomes their weaknesses.

Author Manuscript Author Manuscript Author Manuscript Author Manuscript

F. Comparison with the Other Prostate Segmentation Methods

We first compared our method with the level set based segmentation method and provided the segmentation results in Fig. 13. For initialization of the level set method and our method, we asked the user to draw a box to warp the prostate and to draw the prostate and non-prostate circles, respectively. Then we adopted the level set based segmentation method and our random walk based method for the segmentation. The random walk algorithm obtained the prostate contour that is close to the gold standard, while the level set method produces the segmentation leaks.

We then compared our method with the other segmentation methods.[27, 29, 34, 38] The results are shown in Table II, where DSC is represented by the mean (standard deviation) and the size of the image is represented by the length × width (number of slices). In Table II, our method can achieve a mean DSC of 91.0%, which is higher than the 89.7% of the method[38], 90.81% of the method[34], and 90.3% of the method[29]. Although our DSC is slightly lower for the whole prostate region compared with the method[27], our method has higher DSC for the apex region and mid-gland region. Our standard deviation is also the lowest among these methods, except for the method[34]. The standard deviation of the method[34] is low because it contains only five images. The higher DSC values prove that our method can achieve higher and more stable segmentation performance than the compared methods. From the perspective of efficiency, our method costs about seven minutes for the segmentation on one patient, and which is longer than the other methods. This is because the size of the image to be segmented in our database is large and the number of slices is also large. For example, the method[27] costs four minutes for segmentation, and the size of the image is 136×165 pixels and the number of slices for one patient is from seven to 14, while our image is 448×448 pixels and there are 350 slices required to be segmented for one patient. Not only is the size of our image three times larger than the size of the image in the method[27], but our slice number is also far greater than that in the method[27]. Although the size of the database image and the number of slices in the method[29] are the same as that using our method, it needs a user to draw two, orthogonal bounding boxes and segment the prostate within the boxes.

G. Robustness of our Method

We demonstrate the robustness of our method in term of user interactions by comparing the proposed method with the method.[41] We randomly choose five patients and use the method[41] and our method for segmentation. Our method needs the user to draw the prostate circle and non-prostate circle while the method[41] needs the user to pick up 12 points, including six foreground and six background points, after which the fore- and background points are fitted with two, closed B-spline curves for more seed points. For a more fair comparison, we select the optimized parameters for the method[41] by using segmentation experiments in the same manner. To test the robustness, the user draws different circles for our method and marks different points for the method[41] for ten times, respectively. According to the initial points or circles, we use the method[41] and our method to segment the 3D prostate ten times. The comparison results are shown in Fig. 14. The DSC from our method is stable while the one obtained by the method[41] varies significantly. This illustrates that our method is not affected by the initialization, but that the method[41] is sensitive to the initial seed points.

Author Manuscript Author Manuscript Author Manuscript Author Manuscript

Then we test the robustness of our method compared to the manual segmentations. We evaluated our segmented results using another manual segmentation gold standard obtained by another radiologist. The segmentation results are shown in Table III. In Table III, we can see that we obtain a DSC of 85.4 ± 3.3% between the segmented prostates based on the first radiologist and manual segmentation from the second radiologist. And for the three sub-regions, *i.e.* apex, mid-gland, and base regions, we still achieve a DSC of 78.7 ± 7.7, 90.2 ± 3.2, and 81.4 ± 6.3, respectively. These good results prove the robustness and effectiveness of our method.

IV. DISCUSSION

We describe a semi-automatic segmentation algorithm for the prostate in 3D ultrasound images. The method is initialized with the user determining the start and end slices containing the prostate and drawing the prostate and non-prostate seed circles on the mid-gland slice, and which then automatically segments the prostate on other slices by using a context-classification based, random walk algorithm.

The advantage of our method is that we involve the random walk algorithm for the 3D prostate segmentation and use the combined context-classification information to more accurately locate the seed points for improving the segmentation performance. The random walk algorithm can formulate the segmentation problem on a graph in order to avoid the discretization errors. The algorithm assigns a label to each pixel on the image according to its probability of belonging to the object and it can thus avoid the segmentation leakage and shrinking bias. By comparing with the level set based segmentation method, we can see that the random walk can obtain good segmentation performance. By combining context and classification information, the method can more accurately find fore- and background seed points. The context information from the morphology mask can not only describe the patient-specific characteristics but can also consider the changes between the segmented prostate on the adjacent slice. The classification information from the decision tree classifier can reflect the population-based prior knowledge. However, it is difficult to achieve good segmentation results by using only one of them. By fusing the context and classification information together, we can achieve the discriminative information required to determine the location of the seed points. With more accurate seed points, the random walk algorithm can improve the segmentation result. Experimental results show that the proposed method is effective. It outperforms not only the CO-RW and CL-RW methods, but also the other prostate segmentation methods[27, 29, 34, 38].

The two parameters which are determined by the segmentation experiments do not have a significant effect on the segmentation performance. The comparison results of user interactions demonstrated that our interaction type is more stable than that of the method[41]. The proposed method takes about seven minutes to segment one prostate volume (448×448×350) after the user interaction using MATLAB code in a desktop computer with 32 GB RAM and 3.40 GHz processor. Our method trades speed for a better segmentation performance and fewer user interactions. The method achieved a relatively high and stable segmentation accuracy on the clinic images compared with the manual segmentation by clinically experienced radiologists. Although the segmentation efficiency is not a design

Author Manuscript Author Manuscript Author Manuscript Author Manuscript

criteria, the proposed method can be accelerated and optimized by reducing the size of an image with the use of superpixel and by using parallel processing methods to improve the efficiency in the future.

V. CONCLUSION

In this manuscript, we proposed a semi-automatic, context-classification based random walk algorithm for prostate segmentation of 3D ultrasound images. The method changes the original 3D segmentation problem into a sequence of 2D segmentation sub-problems for a fast segmentation. After a user interaction on the mid-gland slice, the algorithm can automatically segment the 3D prostate slice by slice. Because a random walk algorithm can be sensitive to the location of seed points, it is important to choose these seed points. We combine the context information representing the patient-specific characteristics and classification information representing the population characteristics to automatically acquire the seed points for the random walk algorithm on the other slices except the mid-gland slice. Therefore, being different from the existing hybrid methods, we combine the patient-specific characteristics and population characteristics together to better characterize the patient and adopt the random walk algorithm for more accurate segmentation of the prostate because it can avoid segmentation leakage and shrinking bias. Experimental results show that our method is effective and robust compared to the other methods. The segmentation method can be applied in a variety of prostate-related applications including ultrasound-guided biopsy, diagnosis, and prostate therapy.

Acknowledgments

This work was partially supported by NIH grants CA156775, CA176684, and CA204254, and Georgia Research Alliance Distinguished Scientists Award.

References

1. Siegel RL, Miller KD, Jemal A. Cancer statistics, 2016. CA: A cancer journal for clinicians. 2015; 66:7–30.
2. Tong S, Cardinal HN, McLoughlin RF, Downey DB, Fenster A. Intra-and inter-observer variability and reliability of prostate volume measurement via two-dimensional and three-dimensional ultrasound imaging. Ultrasound in medicine & biology. 1998; 24:673–681. [PubMed: 9695270]
3. Fenster A, Downey DB. Three-dimensional ultrasound imaging of the prostate. Medical Imaging'99. 1999. International Society for Optics and Photonics. 1999:2–11.
4. Ghose S, Oliver A, Martí R, Lladó X, Vilanova JC, Freixenet J, Mitra J, Sidibé D, Meriaudeau F. A survey of prostate segmentation methodologies in ultrasound, magnetic resonance and computed tomography images. Computer Methods and Programs in Biomedicine. 2012; 108:262–287. [PubMed: 22739209]
5. Hodge AC, Fenster A, Downey DB, Ladak HM. Prostate boundary segmentation from ultrasound images using 2D active shape models: Optimisation and extension to 3D. Computer Methods and Programs in Biomedicine. 2006; 84:99–113. [PubMed: 16930764]
6. Hodge, AC., Ladak, HM. 3D prostate boundary segmentation from ultrasound images using 2D active shape models; Conf Proc IEEE Eng Med Biol Soc; 2006. p. 2337-2340.
7. Zhang Y, Matuszewski BJ, Histace A, Precioso F, Kilgallon J, Moore C. Boundary Delineation in Prostate Imaging Using Active Contour Segmentation Method with Interactively Defined Object Regions. Prostate Cancer Imaging: Computer-Aided Diagnosis, Prognosis, and Intervention. 2010:131–142.

Author Manuscript Author Manuscript Author Manuscript Author Manuscript

8. Mahdavi S, Salcudean SE. 3D Prostate Segmentation based on Ellipsoid Fitting, Image Tapering and Warping. Engineering in Medicine and Biology Society. 2008:2988–2991.
9. Mahdavi S, Morris WJ, Spadinger I, Chng N, Goksel O, Salcudean SE. 3D Prostate Segmentation in Ultrasound Images Based on Tapered and Deformed Ellipsoids. Medical Image Computing and Computer-Assisted Intervention. 2009:960–967. [PubMed: 20426204]
10. Li B, Patil AV, Hossack JA, Acton ST. 3D segmentation of the prostate via Poisson inverse gradient initialization. IEEE International Conference on Image Processing. 2007; 5:V-25.
11. Hu N, Downey DB, Fenster A, Ladak HM. Prostate boundary segmentation from 3D ultrasound images. Medical Physics. 2003; 30:1648–1659. [PubMed: 12906182]
12. Hu, N., Downey, DB., Fenster, A., Ladak, HM. Prostate surface segmentation from 3D ultrasound images; Biomedical Imaging, 2002, Proceedings. 2002 IEEE International Symposium on; 2002. p. 613-616.
13. Ghanei A, Soltanian-Zadeh H, Ratkewicz A, Yin FF. A three-dimensional deformable model for segmentation of human prostate from ultrasound images. Medical Physics. 2001; 28:2147–2153. [PubMed: 11695777]
14. Qiu W, Rajchl M, Guo F, Sun Y, Ukwatta E, Fenster A, Yuan J. 3D Prostate TRUS Segmentation Using Globally Optimized Volume-Preserving Prior. Medical Image Computing and Computer-Assisted Intervention. 2014:796–803. [PubMed: 25333192]
15. Qiu W, Yuan J, Ukwatta E, Sun Y, Rajchl M, Fenster A. Prostate Segmentation: An Efficient Convex Optimization Approach with Axial Symmetry Using 3D TRUS and MR Images. Medical Imaging, IEEE Transactions on. 2014; 33:947–960.
16. Qiu W, Yuan J, Ukwatta E, Tessier D, Fenster A. Rotational-slice-Based prostate segmentation using level set with shape constraint for 3D end-firing TRUS guided biopsy. Med Image Comput Comput Assist Interv. 2012:537–544. [PubMed: 23285593]
17. Qiu W, Yuan J, Ukwatta E, Tessier D, Fenster A. Three-dimensional prostate segmentation using level set with shape constraint based on rotational slices for 3D end-firing TRUS guided biopsy. Medical Physics. 2013; 40:072903. [PubMed: 23822454]
18. Qiu W, Yuan J, Ukwatta E, Tessier D, Fenster A. Prostate Segmentation in 3D TRUS Using Convex Optimization with Shape Constraint. Medical Imaging 2013: Image Processing. 2013:866943–866943.
19. Yuan, J., Qiu, W., Ukwatta, E., Rajchl, M., Tai, XC., Fenster, A. Efficient 3D Endfiring TRUS Prostate Segmentation with Globally Optimized Rotational Symmetry; Proceedings of the IEEE Conference on Computer Vision and Pattern Recognition; 2013. p. 2211-2218.
20. Ding M, Chiu B, Gyacskov I, Yuan X, Drangova M, Downey DB, Fenster A. Fast prostate segmentation in 3D TRUS images based on continuity constraint using an autoregressive model. Med Phys. 2007; 34:4109–4125. [PubMed: 18072477]
21. Ding, M., Gyacskov, I., Yuan, X., Drangova, M., Fenster, A., Downey, DB. Slice-Based Prostate Segmentation in 3D US Images Using Continuity Constraint; Conf Proc IEEE Eng Med Biol Soc; 2005. p. 662-665.
22. Ding M, Chen C, Wang Y, Gyacskov I, Fenster A. Prostate segmentation in 3D US images using the Cardinal-spline based discrete dynamic contour. Medical Imaging 2003. International Society for Optics and Photonics. 2003:69–76.
23. Wang Y, Cardinal HN, Downey DB, Fenster A. Semiautomatic three-dimensional segmentation of the prostate using two-dimensional ultrasound images. Medical Physics. 2003; 30:887–897. [PubMed: 12772997]
24. Noble JA, Boukerroui D. Ultrasound image segmentation: a survey. Medical Imaging, IEEE Transactions on. 2006; 25:987–1010.
25. Heimann T, Baumhauer M, Impendörfer T, Mainer HP, Wolf I. Prostate segmentation from 3D transrectal ultrasound using statistical shape models and various appearance models. Medical Imaging. International Society for Optics and Photonics. 2008:69141P–69141P.
26. Shoo F, Ling KV, Phi L, Ng WS, Xiao D. Efficient 3d prostate surface detection for ultrasound guided robotic biopsy. International Journal of Humanoid Robotics. 2006; 3:439–461.

Author Manuscript Author Manuscript Author Manuscript Author Manuscript

27. Nouranian S, Mahdavi SS, Spadinger I, Morris WJ, Salcudean SE, Abolmaesumi P. A Multi-Atlas-Based Segmentation Framework for Prostate Brachytherapy. Medical Imaging, IEEE Transactions on. 2015; 34:950–961.
28. Yang X, Fei B. 3D Prostate Segmentation of Ultrasound Images Combining Longitudinal Image Registration and Machine Learning. SPIE Medical Imaging. International Society for Optics and Photonics. 2012:83162O–83162O.
29. Akbari H, Fei B. 3D ultrasound image segmentation using wavelet support vector machines. Med Phys. 2012; 39:2972–2984. [PubMed: 22755682]
30. Akbari H, Yang X, Halig LV, Fei B. 3D Segmentation of Prostate Ultrasound images Using Wavelet Transform. Proc SPIE. 2011; 7962:79622K.
31. Fei B, Master V, Nieh P, Akbari H, Yang X, Fenster A, Schuster D. A PET/CT directed, 3D ultrasound-guided biopsy system for prostate cancer. Prostate Cancer Imaging. Image Analysis and Image-Guided Interventions. 2011:100–108.
32. Fei B, Schuster DM, Master V, Akbari H, Fenster A, Nieh P. A molecular image-directed, 3D ultrasound-guided biopsy system for the prostate. SPIE Medical Imaging. 2012. International Society for Optics and Photonics. 2012:831613–831613.
33. Yang F, Suri J, Fenster A. Segmentation of prostate from 3-D ultrasound volumes using shape and intensity priors in level set framework. Engineering in Medicine and Biology Society. 2006:2341–2344.
34. Yang X, Schuster D, Master V, Nieh P, Fenster A, Fei B. Automatic 3D Segmentation of Ultrasound Images Using Atlas Registration and Statistical Texture Prior. SPIE Medical Imaging. 2011:796432–796432.
35. Zhan Y, Shen D. Deformable segmentation of 3-D ultrasound prostate images using statistical texture matching method. IEEE Trans Med Imaging. 2006; 25:256–272. [PubMed: 16524083]
36. Zhan Y, Shen D. Automated segmentation of 3D US prostate images using statistical texture-based matching method. Medical Image Computing and Computer-Assisted Intervention. 2003:688–696.
37. Zhan Y, Shen D. An efficient method for deformable segmentation of 3D US prostate images. Medical Imaging and Augmented Reality. 2004:103–112.
38. Yang X, Rossi PJ, Jani AB, Mao H, Curran WJ, Liu T. 3D Transrectal Ultrasound (TRUS) prostate segmentation based on optimal feature learning framework. SPIE Medical Imaging. 2016:97842F–97842F.
39. Grady L. Random walks for image segmentation. Pattern Analysis and Machine Intelligence, IEEE Transactions on. 2006; 28:1768–1783.
40. Peng B, Zhang L, Zhang D. A survey of graph theoretical approaches to image segmentation. Pattern Recognition. 2013; 46:1020–1038.
41. Ma L, Guo R, Tian Z, Venkataraman R, Sarkar S, Liu X, Nieh PT, Master VV, Schuster DM, Fei B. Random walk based segmentation for the prostate on 3D transrectal ultrasound images. Proc. SPIE 9786, Medical Imaging 2016: Image-Guided Procedures, Robotic Interventions, and Modeling. 2016:978607.
42. MacQueen J. Some methods for classification and analysis of multivariate observations. Proceedings of the fifth Berkeley symposium on mathematical statistics and probability. 1967; 1:281–297.
43. Duda, RO., Hart, PE., Stork, DG. Pattern Classification. 2. Wiley; New York: 2007.
44. Ojala T, Pietikäinen M, Harwood D. A comparative study of texture measures with classification based on featured distributions. Pattern recognition. 1996; 29:51–59.
45. Safavian SR, Landgrebe D. A survey of decision tree classifier methodology. IEEE transactions on systems, man, and cybernetics. 1991; 21:660–674.
46. McCrea WH, Whipple FJW. Random Paths in Two and Three Dimensions. Proc. Roy. Soc. Edinburgh. 1940; 60:281–298.
47. Serra J. Introduction to mathematical morphology. Computer vision, graphics, and image processing. 1986; 35:283–305.
48. Fei B, Yang X, Nye JA, Aarsvold JN, Raghunath N, Cervo M, Stark R, Meltzer CC, Votaw JR. MR/PET quantification tools: Registration, segmentation, classification, and MR-based attenuation correction. Medical physics. 2012; 39:6443–6454. [PubMed: 23039679]

Author Manuscript Author Manuscript Author Manuscript Author Manuscript

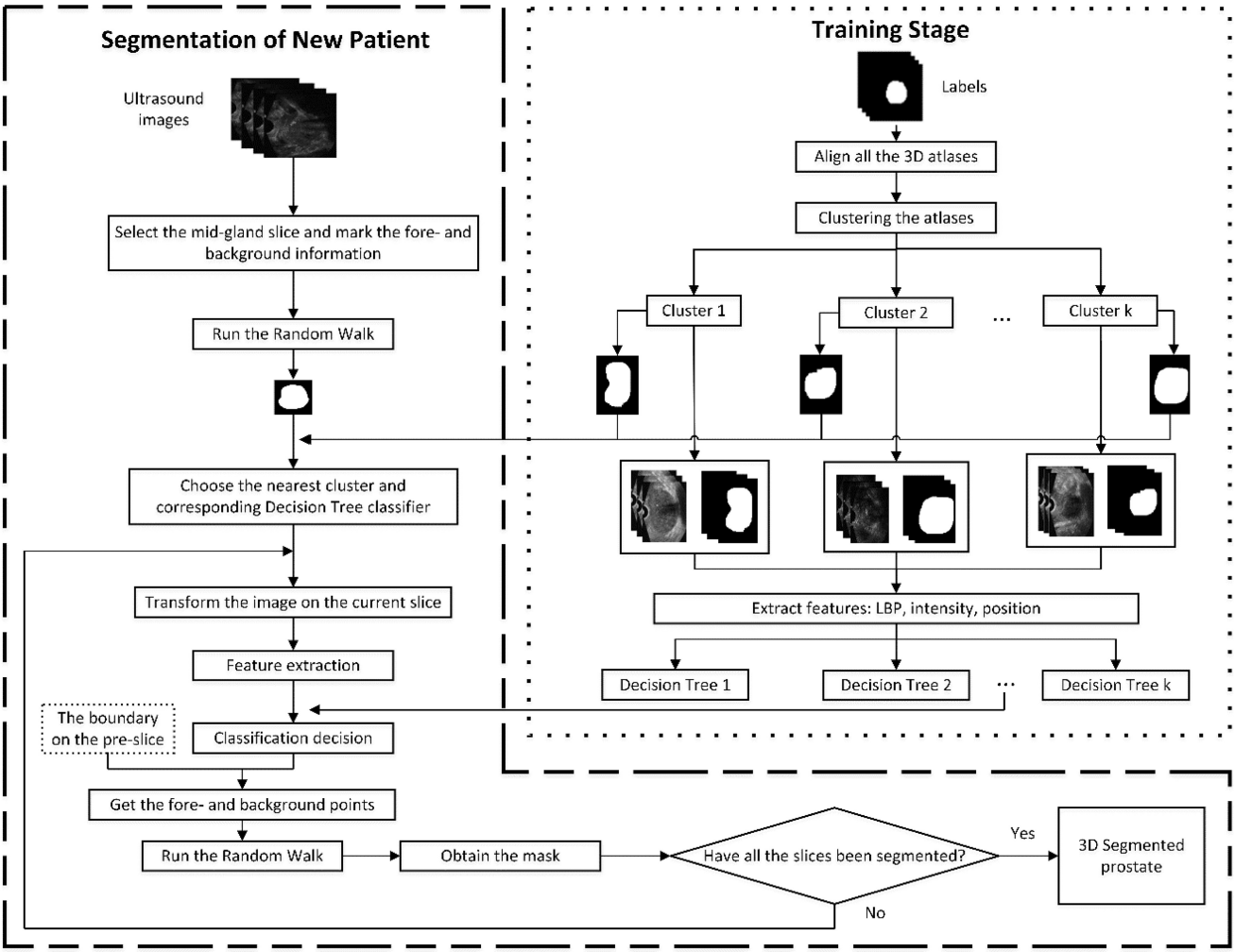

Fig. 1.
Flowchart of the context-classification based, random walk algorithm (C-RW).

Author Manuscript Author Manuscript Author Manuscript Author Manuscript

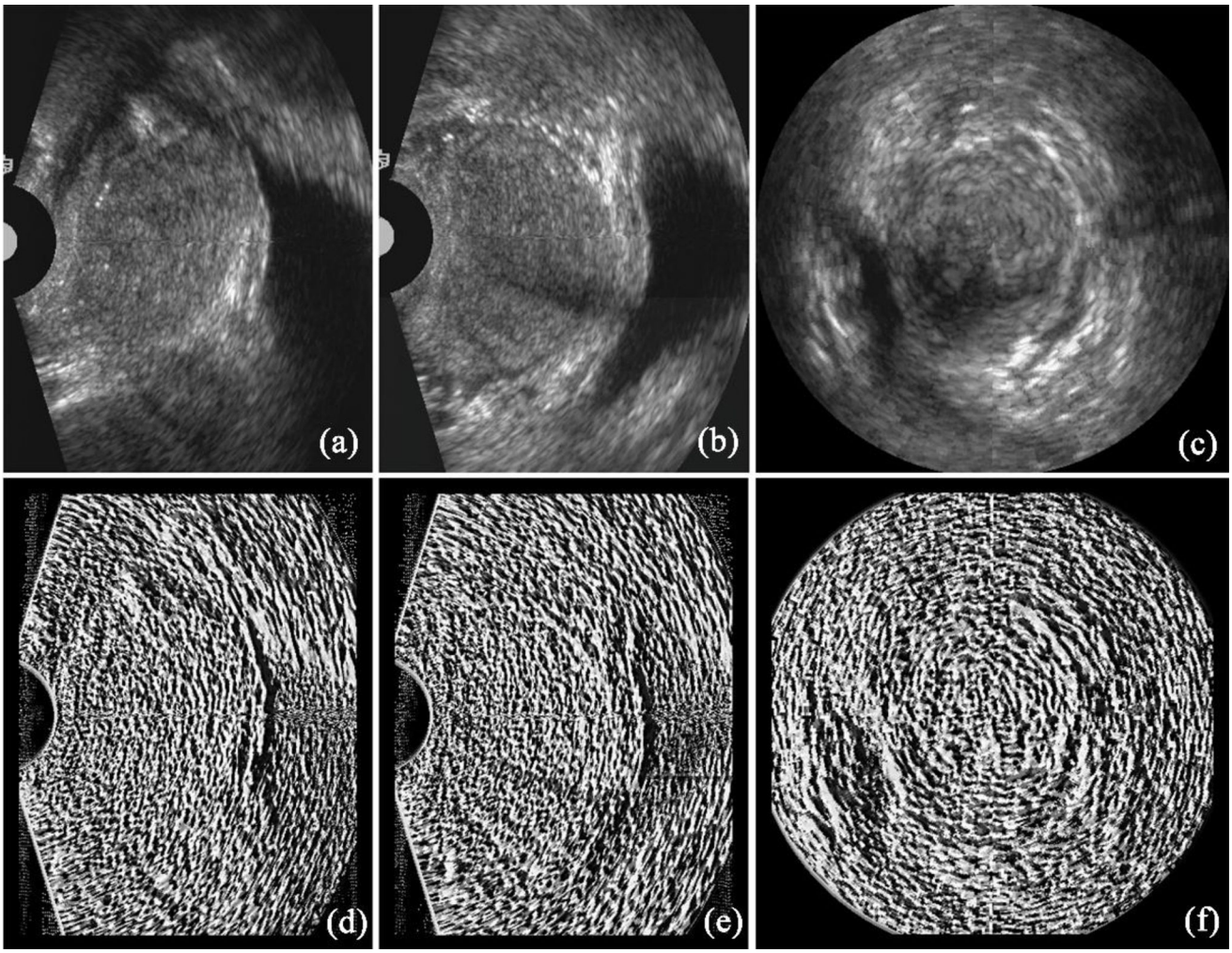

Fig. 2.

Feature extraction using LBP: (a–c) Original images in sagittal, coronal, and transverse directions, respectively. (d–f) Their corresponding LBP feature images.

Author Manuscript Author Manuscript Author Manuscript Author Manuscript

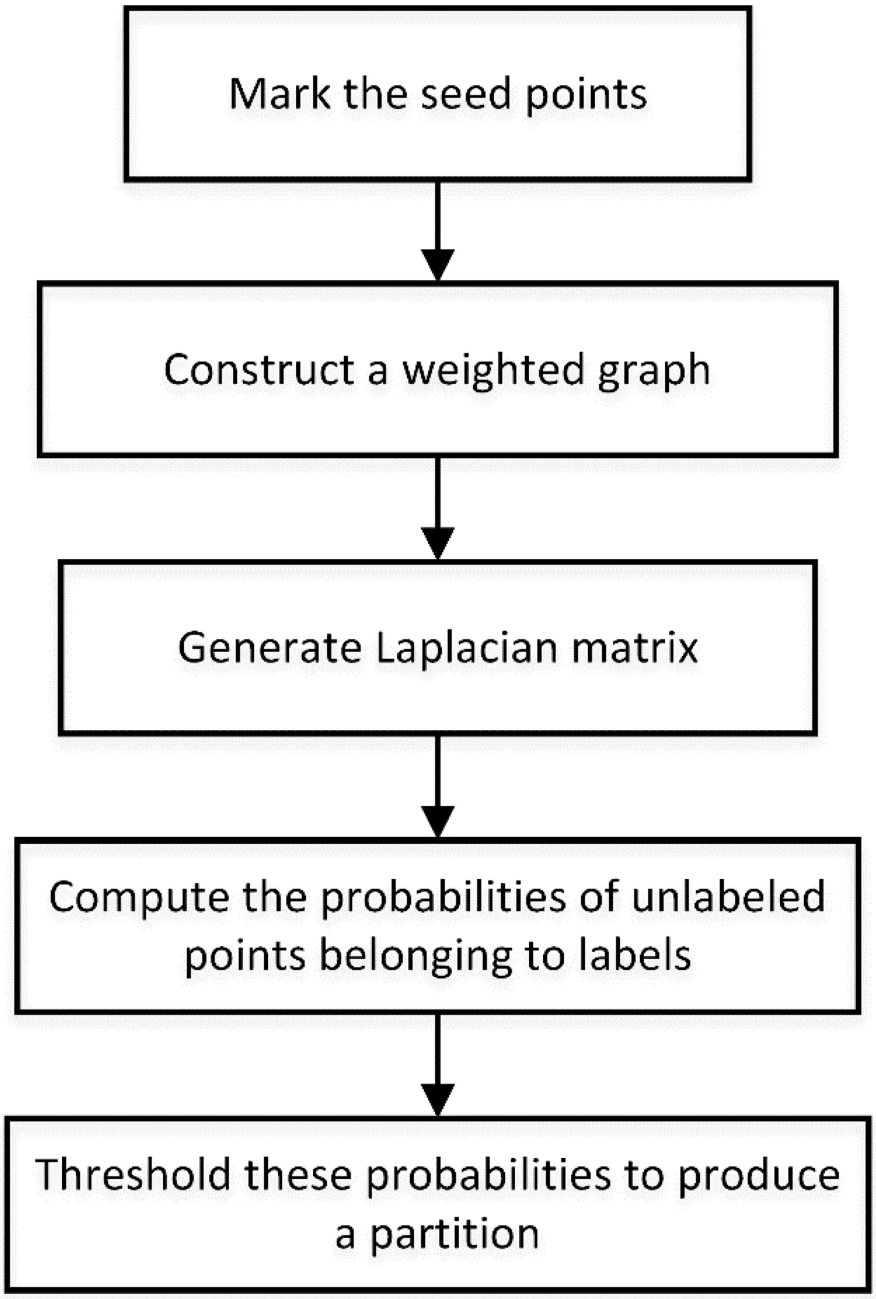

Fig. 3.
Flowchart of random walk for segmentation.

Author Manuscript

Author Manuscript

Author Manuscript

Author Manuscript

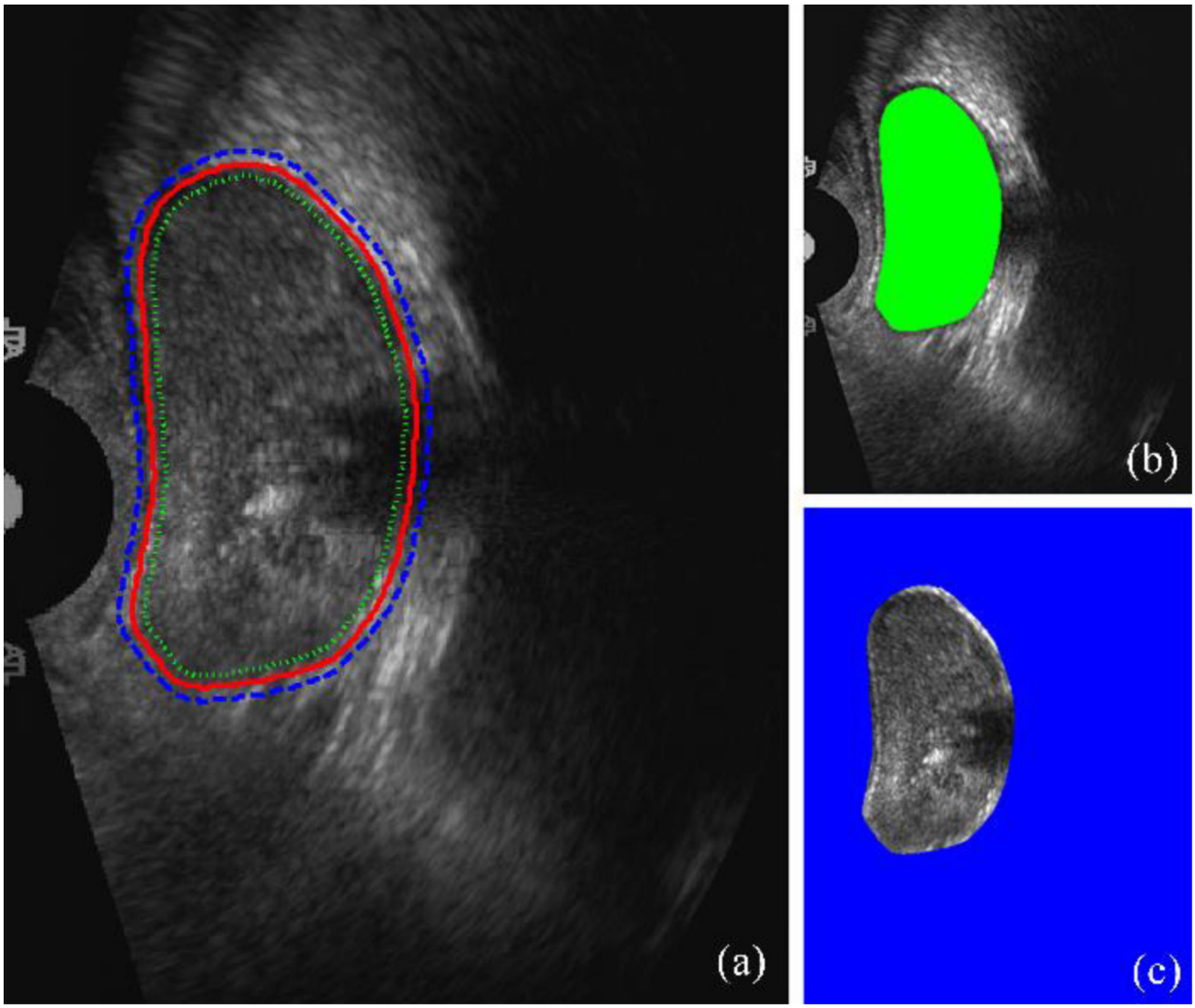

Fig. 4.

Example for determining the fore- and background points according to the context information. (a) The image with the segmented mask on the adjacent slice (solid red line), the shrunk mask (dot green line), and the expanded mask (dash blue line). (b) The image with the foreground points (green region), and (c) The image with the background points (blue region).

Author Manuscript

Author Manuscript

Author Manuscript

Author Manuscript

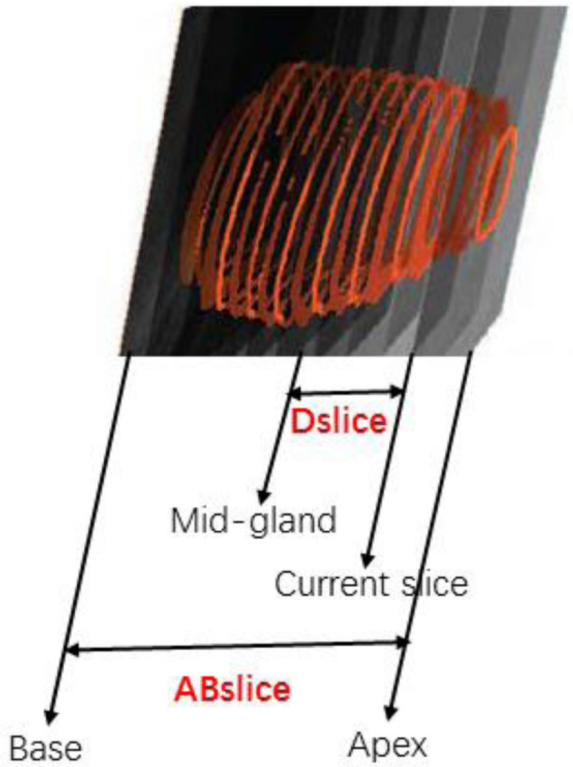

Fig. 5.
Definition of the *Dslice* and *ABslice* for the prostate image slices.

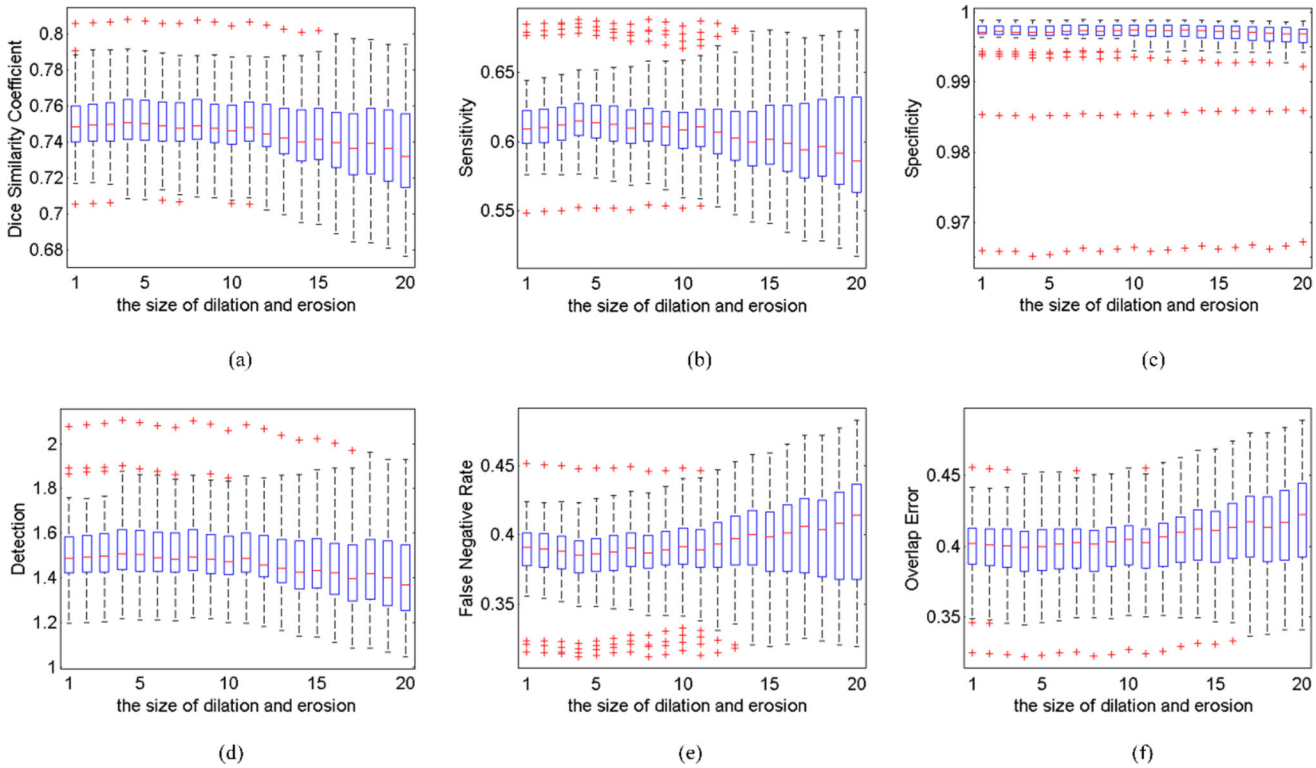

Fig. 6.

Segmentation performance with respect to the size of the dilation and erosion. (a) Dice similarity coefficient, (b) sensitivity, (c) specificity, (d) detection, (e) false negative rate, and (f) overlap error.

Author Manuscript Author Manuscript Author Manuscript Author Manuscript

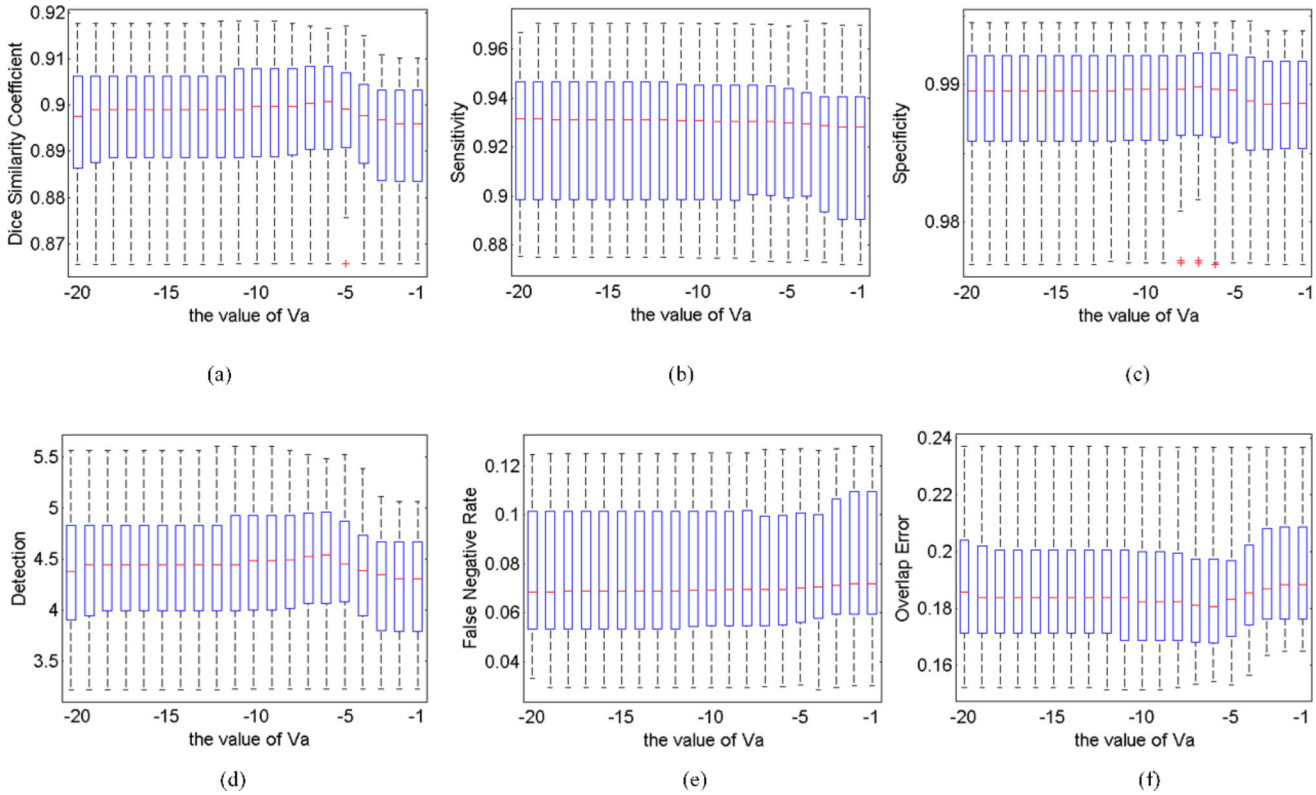

Fig. 7.

Segmentation performance with respect to the value of parameter *Va*. (a) Dice similarity coefficient, (b) sensitivity, (c) specificity, (d) detection, (e) false negative rate, and (f) overlap error.

Author Manuscript
Author Manuscript
Author Manuscript
Author Manuscript

Author Manuscript

Author Manuscript

Author Manuscript

Author Manuscript

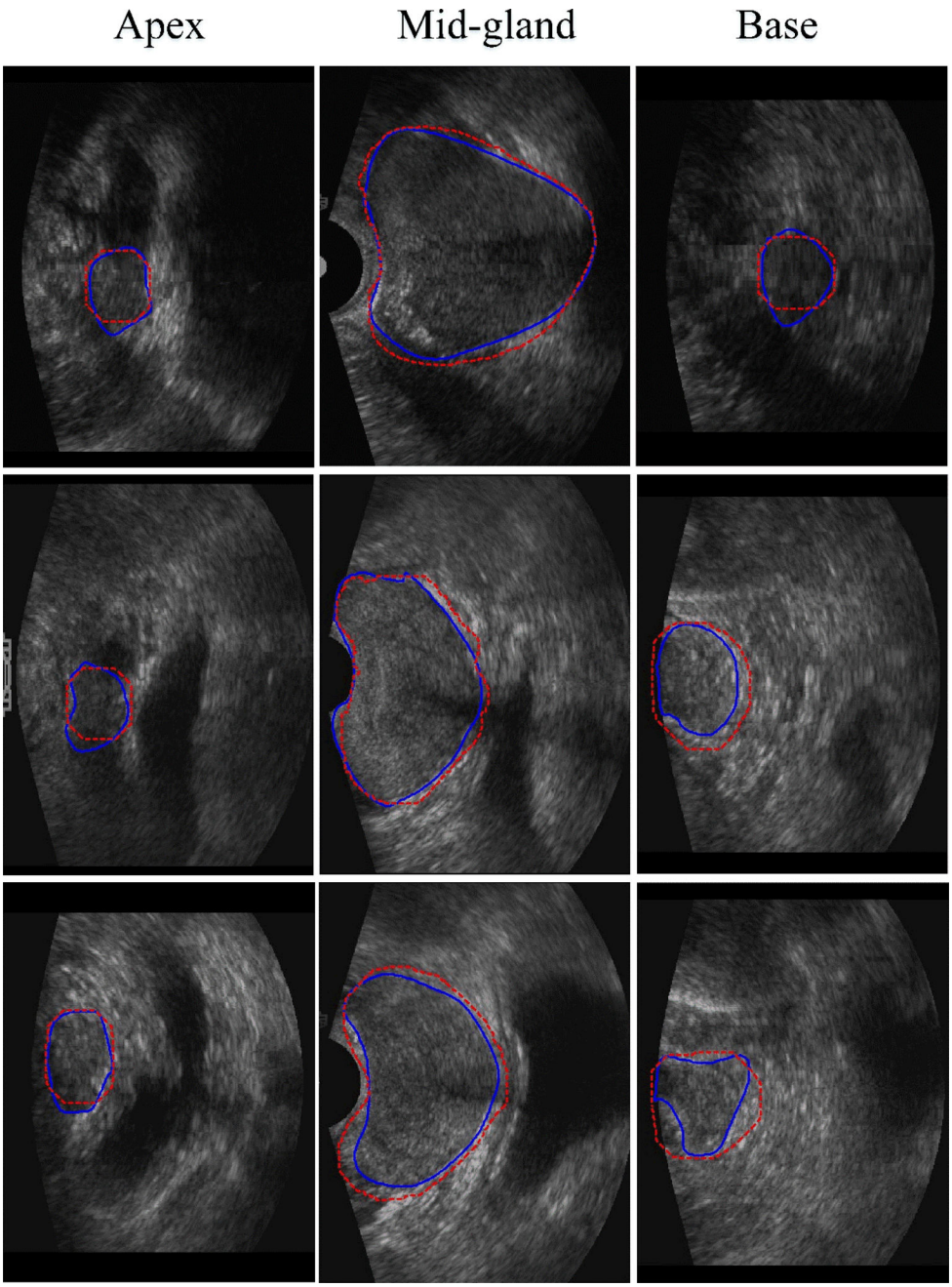

Fig. 8.

Prostate segmentation results of three volumes. The slices are chosen from the base, mid-gland, and apex regions. The solid blue curves are from the manual segmentation of a clinically experienced radiologist, while the dash red curves are from our method.

Author Manuscript

Author Manuscript

Author Manuscript

Author Manuscript

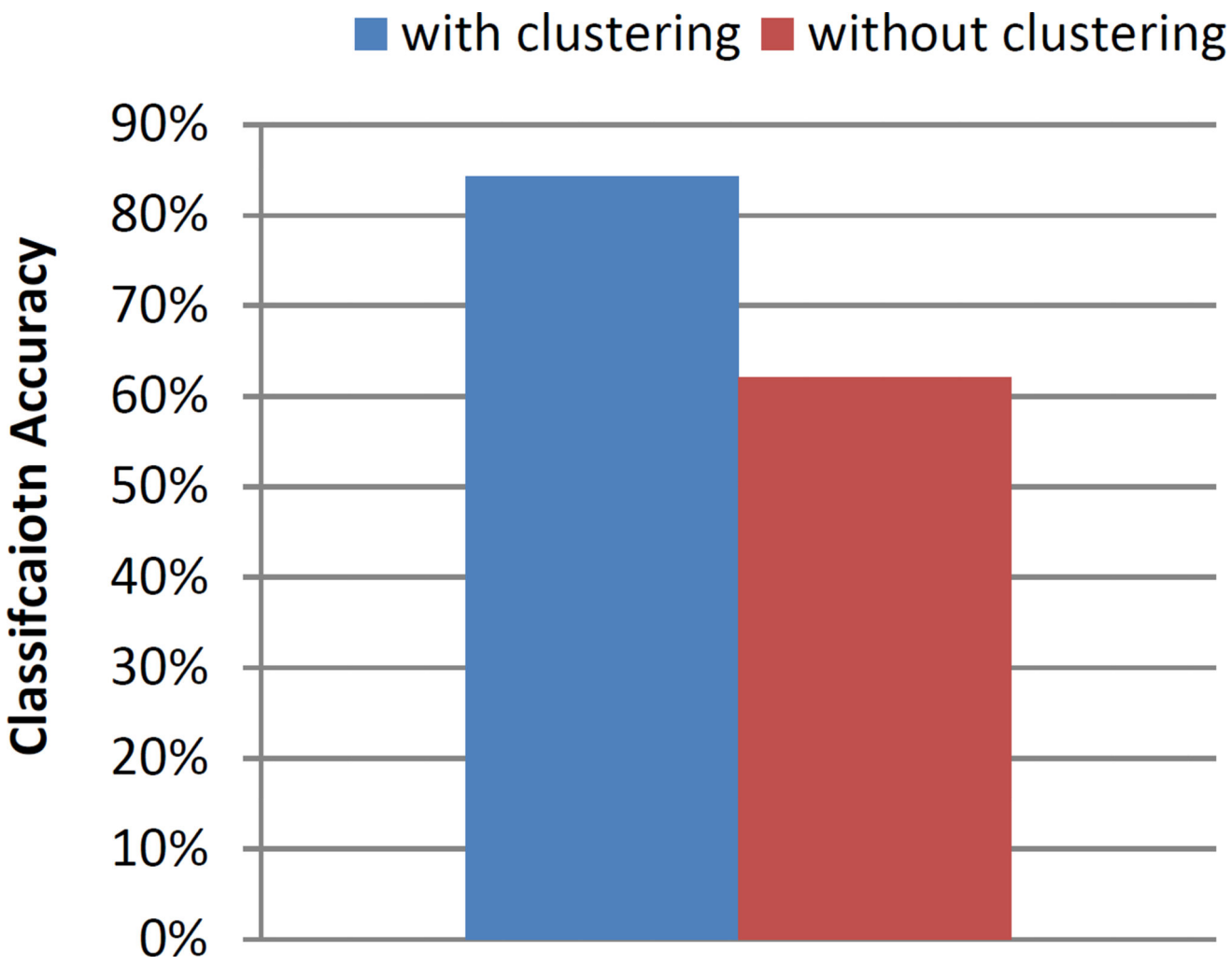

Fig. 9.

Classification accuracy obtained by the training with and without the cluster processing.

Author Manuscript

Author Manuscript

Author Manuscript

Author Manuscript

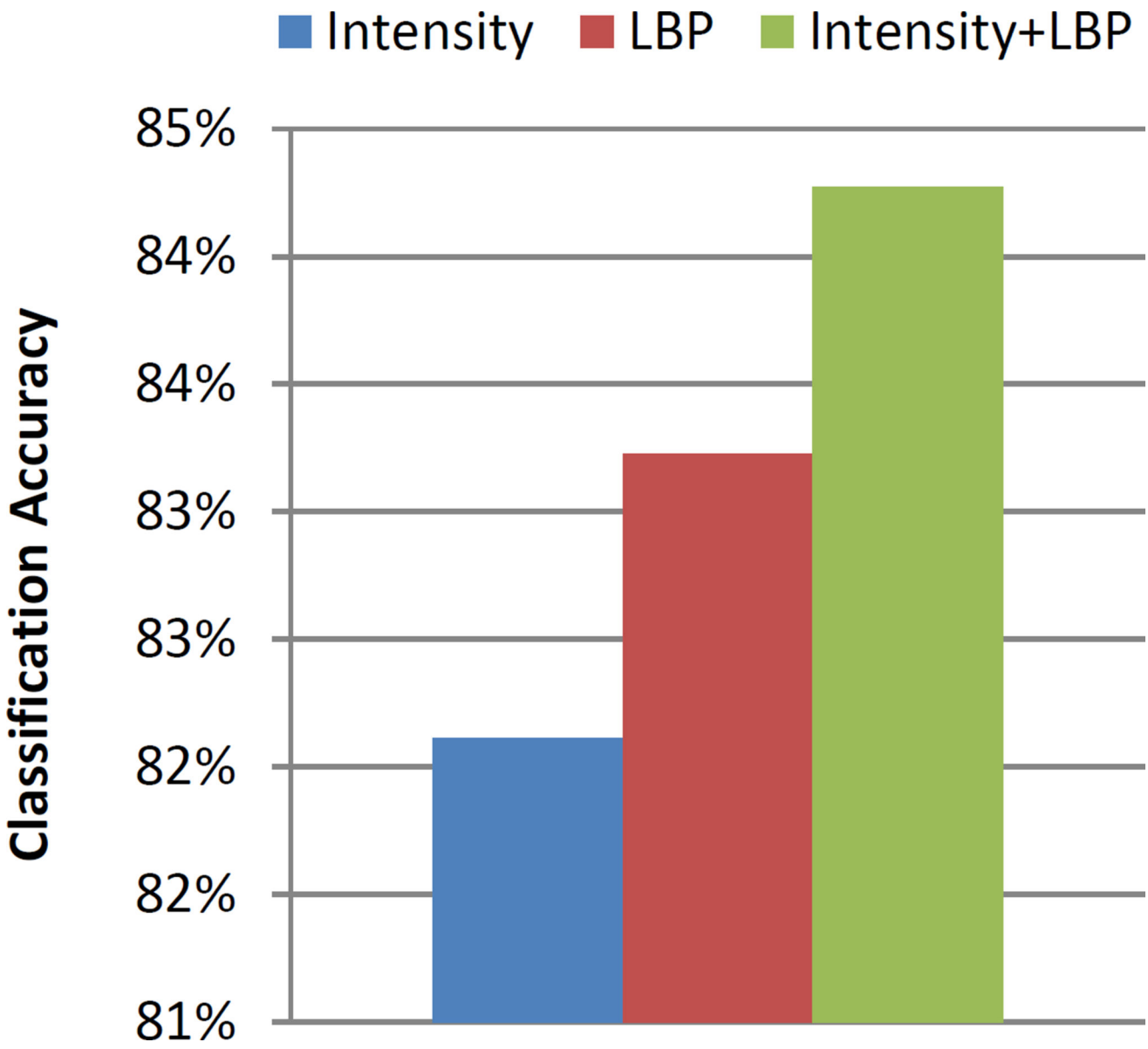

Fig. 10.

The classification accuracy based on the intensity feature only, LBP feature only, and their combined features.

Author Manuscript

Author Manuscript

Author Manuscript

Author Manuscript

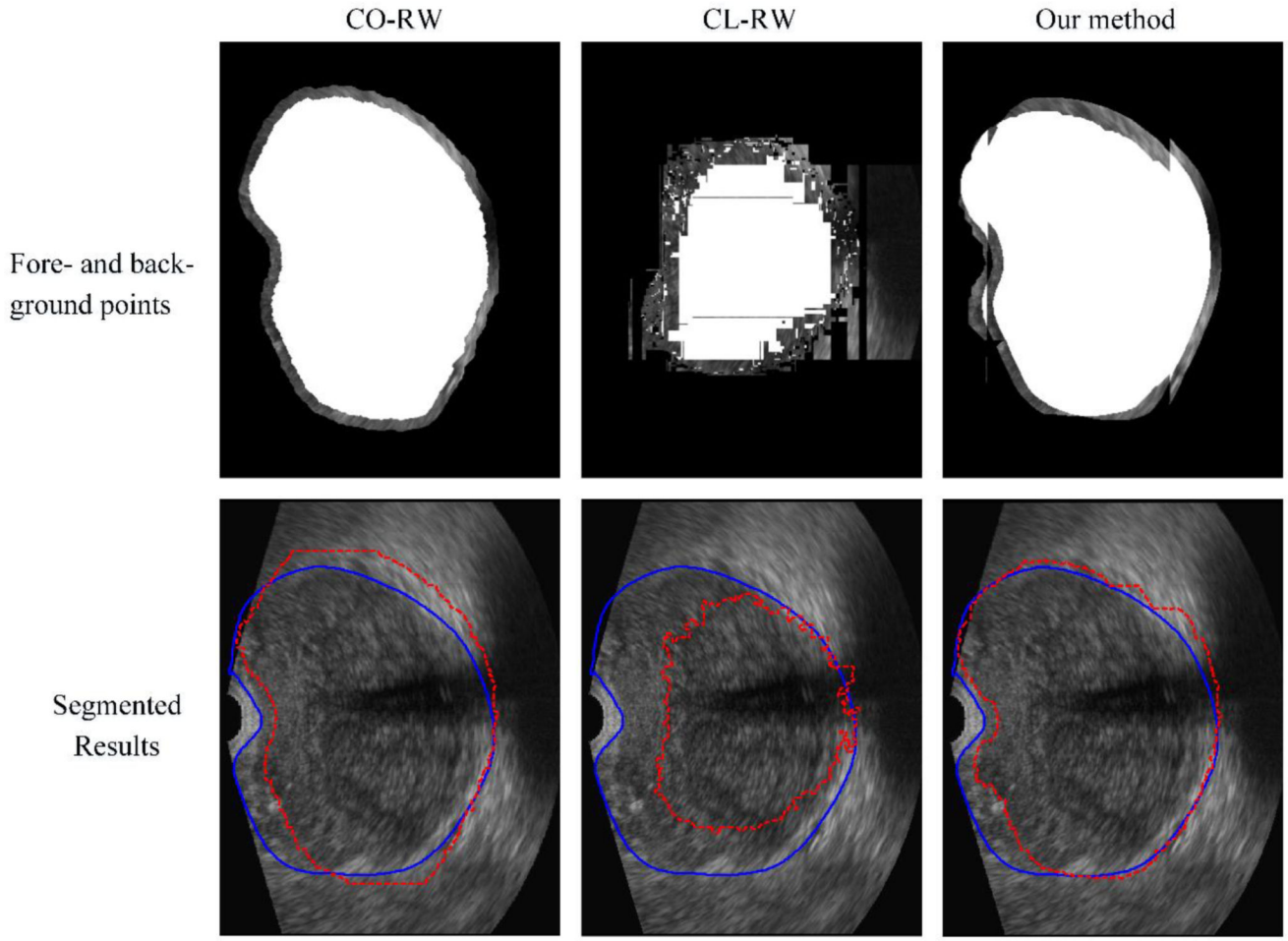

Fig. 11.

The fore- and back- ground points obtained by the context-based initialization, classification-based initialization, and the combined context-classification based initialization, and their corresponding segmentation results, where the white points and the black points indicate the fore- and background points, the segmented prostate is the dash red line, and the manual segmentation is the solid blue line.

Author Manuscript Author Manuscript Author Manuscript Author Manuscript

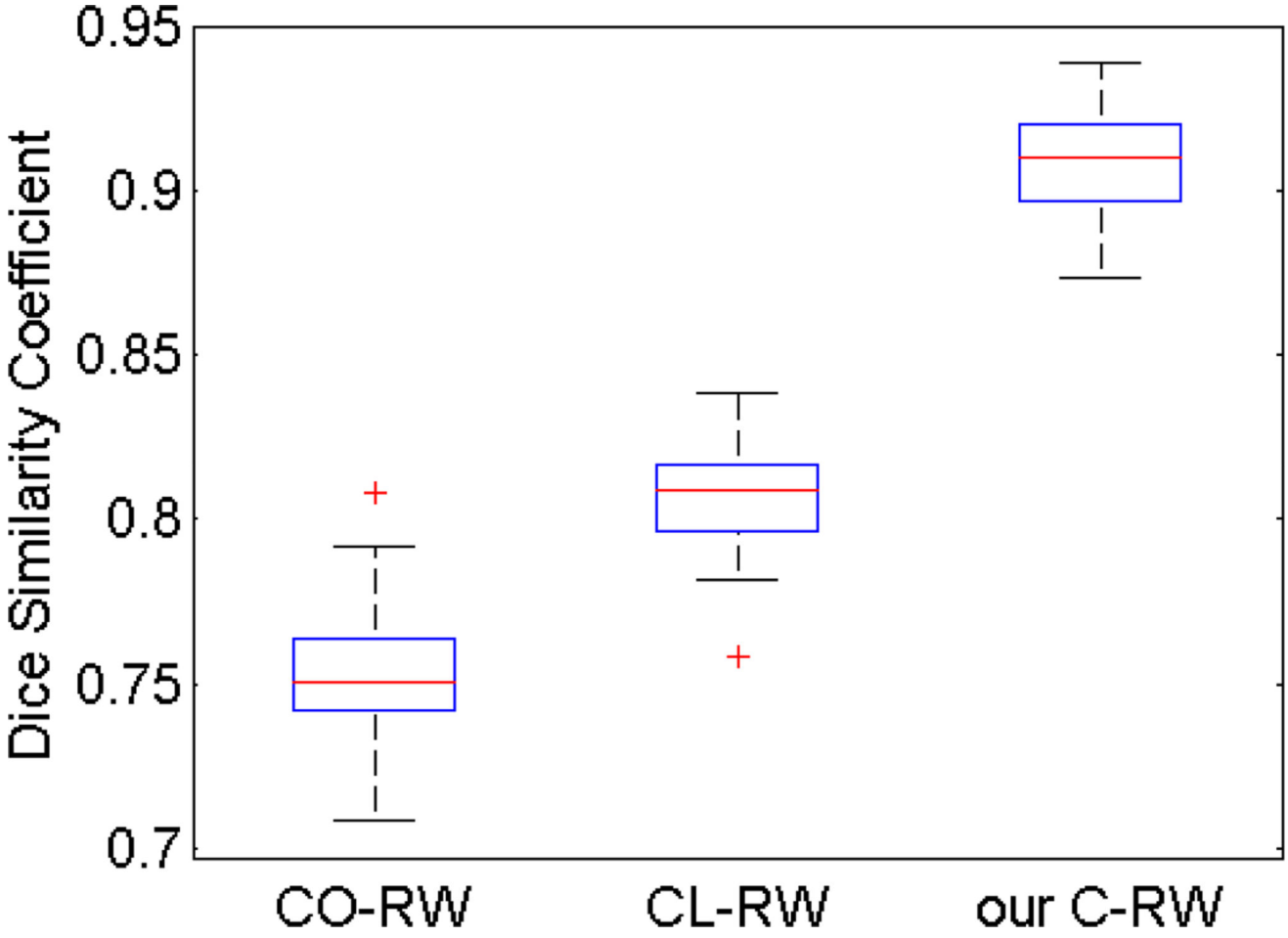

Fig. 12.

Performance comparison among three segmentation approaches: the CO-RW; CL-RW; and our C-RW for 32 volumes.

Author Manuscript

Author Manuscript

Author Manuscript

Author Manuscript

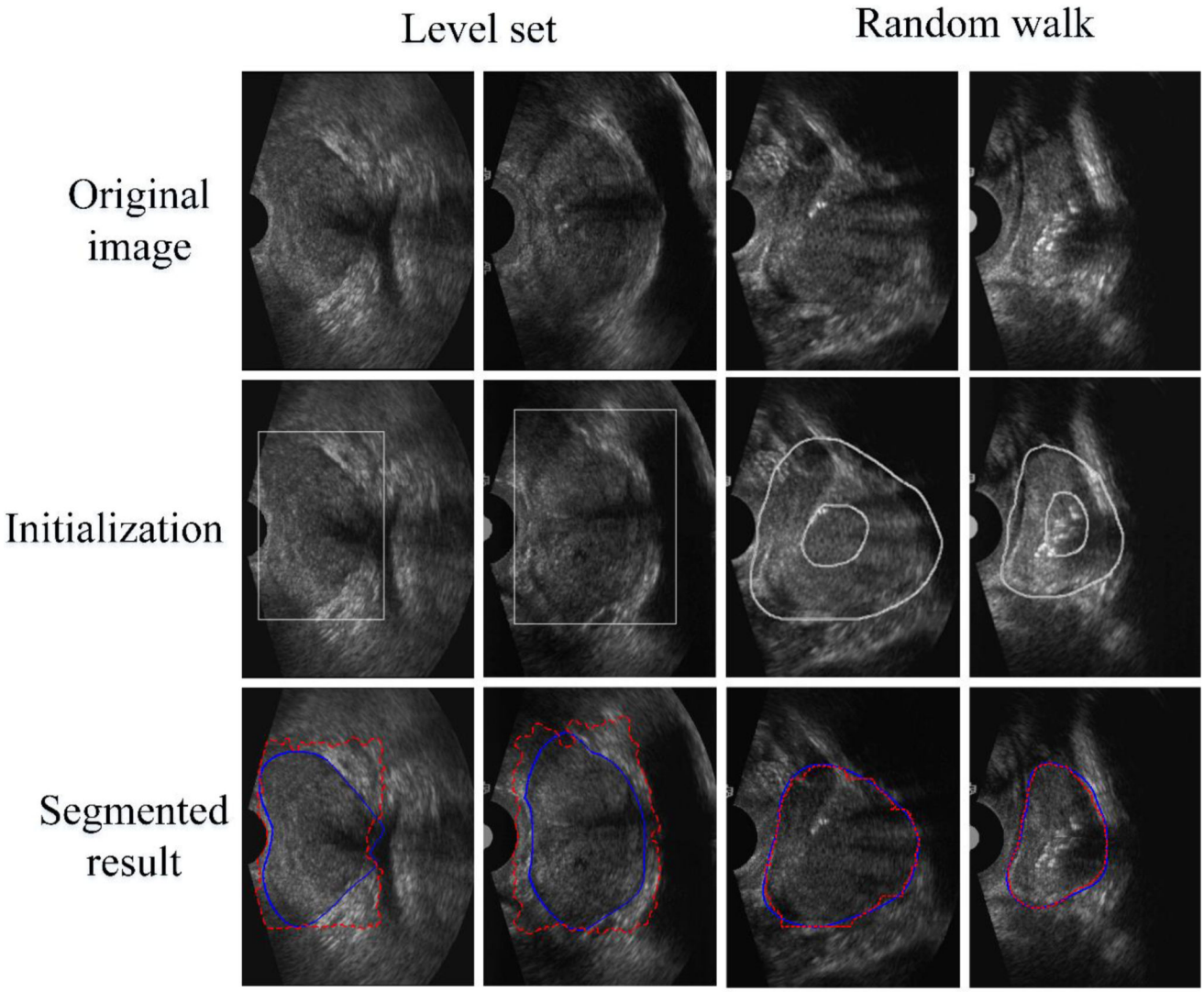

Fig. 13.

Prostate segmentation of the mid-gland slice using the level set method and our random walk algorithm, where the rectangles are drawn manually for the level set method and the inner and outer circles are roughly drawn manually for the random walk algorithm. The segmented prostate is the dash red line and the manual segmentation is the solid blue line.

Author Manuscript

Author Manuscript

Author Manuscript

Author Manuscript

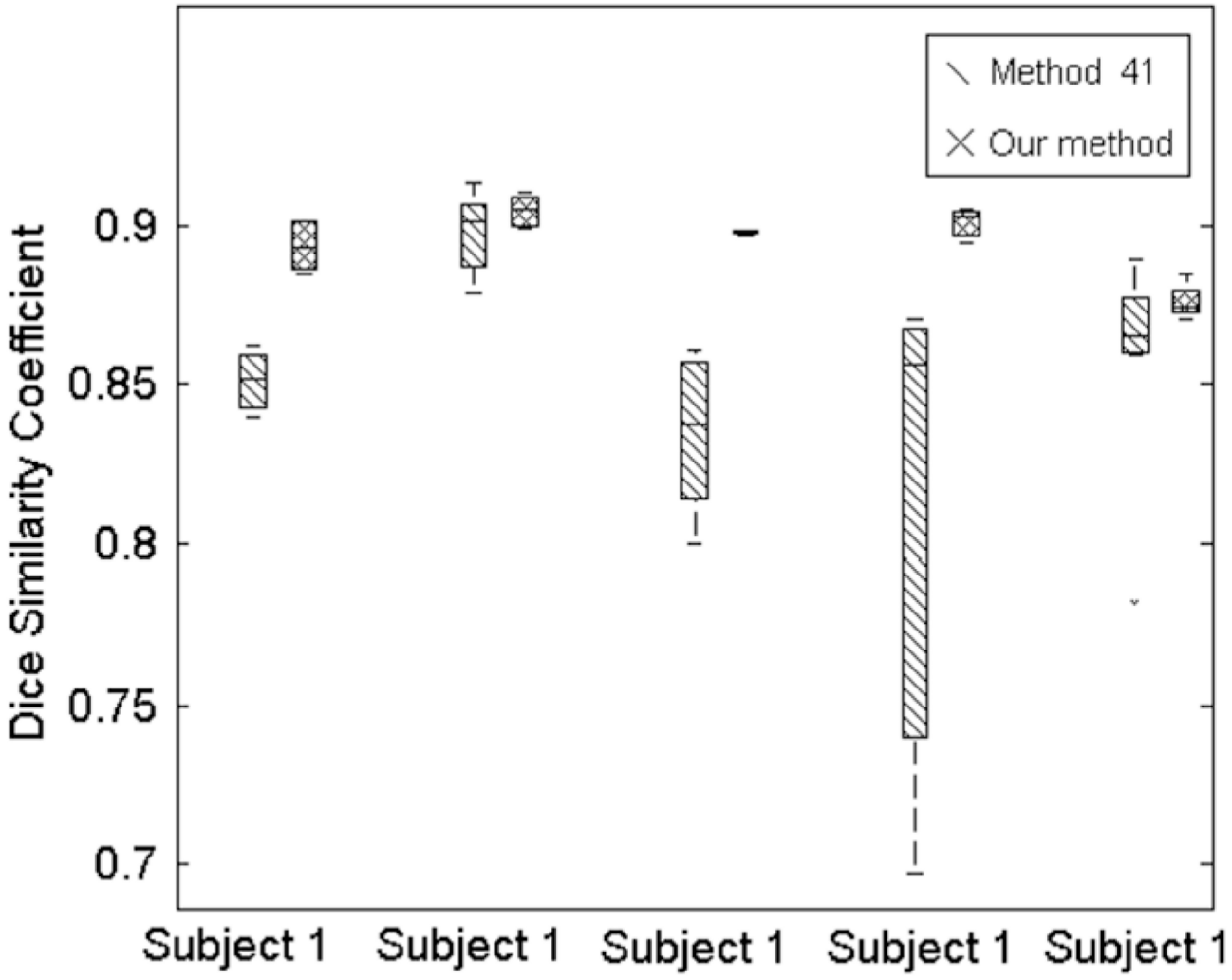

Fig. 14.

Segmentation comparison measured by DSC for different initialization method: The method reported in [41] and our method for the same 5 volumes with 10 times segmentation.

Author Manuscript Author Manuscript Author Manuscript Author Manuscript

TABLE I

Segmentation results for 32 volumes of the whole gland and the three sub-regions (base, mid-gland, and apex).

	DSC (%)	Sensitivity (%)	Specificity (%)	Detection	FNR (%)	OVR (%)	HD (mm)
Apex	88.2±3.1	90.4±6.9	98.5±0. 6	4.0±1.1	9.6±6.9	21.1±4.8	7.9±1.6
Mid-gland	94.0±1.7	93.6±4.0	98.6±0.5	8.3±2.2	6.4±4.0	11.3±2. 9	9.3±1.7
Base	86.8±2.5	91.2±6.5	99.4±0.4	3.4±0.7	8.9±6.5	23.2±3.9	5.6±1.8
Whole gland	91.0±1.6	92.1±4.2	99.0±0.4	5.5±1.1	7.9±4.2	16.6±2.8	8.9±1.4

Author Manuscript Author Manuscript Author Manuscript Author Manuscript

TABLE II

Performance comparison between our method and the other methods.

	DSC (mean and standard deviation)		Database	Image size	Speed
Method[34]	90.81 (1.16)		5	448×448(350)	-
Method[29]	90.3 (2.3)		40	448×448(350)	2–3 min
Method[38]	89.7 (2.3)		10	1024×768 (75)	-
Method[27]	base	91.87 (>6.02)	280	136×165(7–14)	4 min
	mid	93.57 (>4.75)			
	Apex	87.99 (>10.17)			
	whole	91.19 (5.60)			
Proposed method	base	86.8 (2.5)	32	448×448(350)	7 min
	mid	94.0 (1.7)			
	Apex	88.2 (3.1)			
	whole	91.0 (1.6)			

Author Manuscript Author Manuscript Author Manuscript Author Manuscript

TABLE III

Segmentation results of 32 volumes for the whole gland and the three sub-regions (base, mid-gland, and apex) on the second manual segmentation gold standard.

	DSC (%)	Sensitivity (%)	Specificity (%)	Detection	FNR (%)	OVR (%)	HD (mm)
Apex	78.7 ± 7.7	73.7 ± 15.0	98.8 ± 1.0	2.2 ± 1.1	26.3 ± 15.0	34.5 ± 10.4	10.4 ± 5.6
Mid-gland	90.2 ± 3.2	87.1 ± 5.4	98.5 ± 1.1	5.2 ± 2.0	12.9 ± 5.4	17.8 ± 5.3	10.9 ± 3.4
Base	81.4 ± 6.3	84.1 ± 10.4	99.3 ± 0.4	2.4 ± 0.8	15.9 ± 10.4	31.0 ± 8.5	9.5 ± 5.3
Whole gland	85.4 ± 3.3	82.2 ± 6.5	99.0 ± 0.6	3.1 ± 0.9	17.8 ± 6.5	25.4 ± 5.1	10.7 ± 5.2